Journal of Advanced Ceramics
2024, **13**(12): 1974–1984
https://doi.org/10.26599/JAC.2024.9220990
Research Article

Dielectric–magnetic manipulation of reduced graphene oxide permittivity for enhanced electromagnetic wave absorption

Kaili Zhang[1,2,3], Zhen Wang[2,✉], Yuefeng Yan[2], Guansheng Ma[2], Renchao Che[4,✉], Dechang Jia[1,2,3], Xiaoxiao Huang[1,2,3,✉], Yu Zhou[1,2,3]

[1] *State Key Laboratory of Precision Welding & Joining of Materials and Structures, Harbin Institute of Technology, Harbin 150001, China*
[2] *School of Materials Science and Engineering, Harbin Institute of Technology, Harbin 150001, China*
[3] *MIIT Key Laboratory of Advanced Structural-Functional Integration Materials & Green Manufacturing Technology, Harbin Institute of Technology, Harbin 150001, China*
[4] *Laboratory of Advanced Materials, Shanghai Key Lab of Molecular Catalysis and Innovative Materials, Fudan University, Shanghai 200438, China*

Received: August 30, 2024; Revised: September 29, 2024; Accepted: October 16, 2024

Abstract: Graphene is a promising electromagnetic wave absorption (EMWA) material because of its structural designability, controllable electromagnetic properties, and excellent stability. However, the impedance mismatch caused by high conductivity and dielectric properties has seriously hindered the application of graphene in the EMWA field. In this work, based on the dielectric dispersion behavior of ideal broadband absorption as a guide, a Fe microsheet/reduced graphene oxide (Fe/RGO) composite was prepared by simple hydrothermal and thermal reduction methods. The permittivity of RGO is optimized by adjusting the content of anisotropic Fe microsheets, and a balance between attenuation ability and impedance matching is achieved. Theoretical calculations and off-axis electron holography results reveal that the abundant polar sites and heterogeneous interfaces of Fe and RGO enhance the dipole and interface polarizations. The three-dimensional (3D) conductive network structure contributes to multiple reflections of incident electromagnetic waves and conduction loss. The natural and exchange resonances and eddy current loss caused by anisotropic Fe microsheets further increase magnetic loss. Based on the dielectric-magnetic loss mechanism and good impedance matching, Fe/RGO achieves a minimum reflection loss (RL_{min}) of −67.95 dB at 8.48 GHz and a maximum effective absorption bandwidth (EAB_{max}) of 6.91 GHz (11.09–18 GHz) with a low filling content of 10 wt%. In addition, Fe/RGO has excellent radar stealth performance, with a radar cross section (RCS) of −31.21 dBm^2 at 0°. Therefore, the proposed strategy and theoretical analysis provide a reference for the microstructure design, composition, and mechanism analysis of EMWA materials.

Keywords: electromagnetic wave absorption (EMWA); Fe microsheets; reduced graphene oxide (RGO); dielectric–magnetic loss; impedance matching

1 Introduction

With the development of communication technology, electromagnetic pollution is increasingly aggravated due to the wide application of electronic equipment in military and civil fields [1–4]. Electromagnetic radiation not only interferes with the normal operation of equipment but also endangers the environment and human health [5–7]. Therefore, the design and preparation of electromagnetic wave absorption (EMWA) materials is of great significance in civil and military fields [8–12]. The current absorbing materials include ferrites [13], magnetic metals [14], ceramics [15], and polymers [16], but they have several shortcomings, such as impedance mismatching, narrow effective absorption bands and high filling contents, which limit their development in the EMWA field. Carbon materials such as carbon nanotubes [17], graphene [18], carbon fibers [19], carbon black [20], carbon-based aerogels [21], and biomass-derived carbon [22–24] have low densities, high specific surface areas and excellent conductivity characteristics, which can meet the requirements of low thickness, light weight and excellent absorption; thus, these materials have great application prospects in the electromagnetic protection field.

Graphene is a new two-dimensional carbon material with a hexagonal structure composed of carbon atoms in sp^2 hybrid orbitals, which was first obtained by the mechanical stripping method in 2004 [25]. Graphene has unique two-dimensional material properties, such as high thermal conductivity, high carrier mobility, low resistivity, large specific surface area, and excellent chemical stability [26–29]. However, pure graphene is not an ideal microwave absorber because its high electron mobility results in high reflectivity (poor impedance matching characteristics) based on Maxwell theory [30]. In addition, the van der Waals force effect between graphene sheets makes it easy to agglomerate and stack, which also severely deteriorates the overall EMWA performance [31]. More importantly, the single conduction loss or dielectric loss makes it difficult to realize the

✉ Corresponding authors.
E-mail: Z. Wang, hagongdawangzhen@163.com;
R. Che, rcche@fudan.edu.cn;
X. Huang, swliza@hit.edu.cn

broadband and strong absorption. To improve the EMWA performance of graphene, researchers usually compound graphene with other or magnetic loss materials to enhance the electromagnetic attenuation ability. For example, Yan *et al.* [32] successfully fabricated the Fe_3O_4/MoS_2/reduced graphene oxide (RGO)/$Ti_3C_2T_x$ MXene composite by directional freezing and heat treatment methods, in which the incorporation of dielectric/magnetic components improved the synergistic effect of electromagnetic loss. Thus, a minimum reflection loss (RL_{min}) of −66.92 dB (3.61 mm) and a maximum effective absorption bandwidth (EAB_{max}) of 6.08 GHz were achieved. Cao *et al.* [33] reported that a nanocrystalline line-assembled porous hierarchical NiO@$NiFe_2O_4$/RGO heterostructure exhibited good impedance matching and microwave attenuation due to its structural and component advantages. The composite of graphene and magnetic materials can reduce its overall permittivity (ε_r), and its own magnetic properties can increase the permeability (μ_r), which causes it to approach the impedance matching condition to ensure that the incident electromagnetic wave (EMW) enters the absorber to maximize attenuation. Cui *et al.* [34] coated Fe_3O_4 nanoparticles with Nb_2CT_x and RGO sheets, forming a unique hierarchical architecture (RGO/Nb_2CT_x/Fe_3O_4) via hydrothermal and electrostatic self-assembly processes. The introduction of magnetic Fe_3O_4 regulates the dielectric properties of the composite and contributes to its own magnetic loss, which greatly results in electromagnetic synergistic loss and impedance matching. RL_{min} reaches −59.17 dB, and EAB_{max} can reach 6.8 GHz. From the above references, the combination of graphene and magnetic components can improve impedance matching under the synergistic dielectric–magnetic loss effect to increase the EMWA efficiency and broaden the effective absorption bandwidth.

Magnetic loss mechanisms include natural resonance, exchange resonance, and eddy current losses in the GHz band [35,36]. The magnetic loss-type materials mainly include magnetic metals, metal oxides and alloys, which have the advantages of high permeability, low preparation cost, and strong loss [37–39]. Iron (Fe) is the most abundant magnetic metal on Earth and exhibits unique physical and chemical properties and excellent magnetic properties. In addition, Fe has the advantages of simple preparation process and diversity, controllable morphology, low cost, and high yield, making it an excellent choice for EMWA materials [40,41]. Researchers have found that anisotropic magnetic materials can break through the Snoek's limit, thus effectively enhancing the broadband EMWA performance. Magnetic loss absorbers such as Fe chains, FeCo nanochains, Fe@Fe_3C@C chains, FeCo@C nanoflakes, and FeSiAl flakes have high-efficiency EMW loss ability due to their unique anisotropic structure [42–46]. Cai *et al.* [47] designed a unique magnetoelectric bias interface by constructing a bilayer core-shell structure of $NiFe_2O_4$@$BiFeO_3$@olypyrrole (PPy). The heterogeneous interface can induce distinct magnetic pinning of the magnetic moment in ferromagnetic $NiFe_2O_4$ and dielectric pinning of the dipole rotation in PPy, which effectively improves the magnetocrystal-line anisotropy. Moreover, the permittivity and permeability of absorbers can be modulated by the length/diameter ratio, morphology, composition, defects, and crystal phase [48–51]. Although anisotropic magnetic materials greatly improve EMWA properties, their large thickness and high filling content limit their further practical applications. Therefore, the composite of anisotropic magnetic materials and dielectric materials can give full play to electromagnetic loss mechanisms, which improve impedance matching, and the attenuation ability becomes critical to solve the above problems.

In this work, the ideal complex permittivity ranges of the absorbing materials are obtained under broadband effective absorption conditions according to the transmission line theory. Under this guidance, a series of Fe microsheets/reduced graphene oxide (Fe/RGO) composites were successfully prepared by hydrothermal and thermal reduction strategies. The complex permittivity and permeability of Fe/RGO composites are regulated by controlling the mass ratio of Fe and RGO. Fe microsheets are anchored on RGO sheets and connected to each other to form a network structure, which contributes to forming a conductive network and multiple interfaces between Fe and RGO to promote conduction loss and interface polarization. In addition, the abundant defects and polar functional groups in Fe/RGO composite can serve as centers of polarization to induce dipole polarization. The natural and exchange resonances and eddy current loss caused by anisotropic Fe microsheets further enhance the magnetic loss. Based on the dielectric–magnetic loss mechanism and good impedance matching, the obtained Fe/RGO 4 : 1 RL_{min} can reach −67.95 dB with a thickness of 3.47 mm, and EAB_{max} is 6.91 GHz (2.40 mm). Moreover, the optimal radar cross section (RCS) of Fe/RGO 4 : 1 is −31.21 dBm^2 (detection angle 0°). This study not only provides a novel idea for the structural design of graphene-based EMWA materials but also clarifies the dielectric–magnetic loss mechanism of materials.

2 Experimental

2.1 Materials

Graphite powder (325 mesh, ≥ 99.9% purity), ferric nitrate nonahydrate ($Fe(NO_3)_3·9H_2O$, 99.8%), potassium hydroxide (KOH, 99%), and hexadecyl trimethyl ammonium bromide (CTAB, 99%) were obtained from Aladdin Co., Ltd. (China). All the chemicals were of analytical grade (AR) without any further purification.

2.2 Synthesis of Fe microsheet/RGO composites

Graphene oxide (GO) was obtained from graphite by the modified Hummers' method [52]. 0.83 g CTAB and 15 g KOH were dispersed in 10 mL deionized (DI) water and slowly mixed for 1 h to form mixed solution A. 2.02 g $Fe(NO_3)_3·9H_2O$ was dissolved in 10 mL deionized (DI) water to form mixed solution B. Then, the solution A was poured into the solution B and stirred for 2 h. A 10 mg/mL GO solution was slowly added to the above mixed solution and stirred for 3 h. The mixed solution was transferred to an autoclave for hydrothermal reaction (2 h, 240 °C). The product (Fe_2O_3/RGO) was washed with ethanol and DI water. The mixture was frozen for 24 h in a refrigerator and subjected to the freeze-drying process (−50 °C, 0.2 Pa) for 36 h. The resulting Fe_2O_3/RGO was put into a tube furnace and reduced for 2 h at 350 °C (5 °C/min) under a H_2 atmosphere to obtain the final product. The black powder was referred to as Fe/RGO. For comparison, experiments were also carried out with different mass ratios of precursor Fe_2O_3 and GO (1 : 8, 1 : 4, 1 : 2, 1 : 1, 2 : 1, 4 : 1, and 8 : 1), and the corresponding preparation process was consistent with that described above (Table S1 in the Electronic Supplementary Material (ESM)).

2.3 Characterizations

The morphology and microstructure of the samples were obtained by a scanning electron microscope (SEM, ZEISS Merlin Compact) and a high-resolution transmission electron microscope (TEM, Talos F200X). The phase structure was tested by an X-ray diffractometer (XRD, DX-2700). An inductively coupled plasma-mass spectrometer (ICP-MS, NexION 350X) was used to determine the Fe content in samples. The Raman spectra of RGO were recorded via an inVia-Reflex Raman spectroscopy system with a 532 nm laser. The composition and chemical valence state were obtained via an X-ray photoelectron spectrometer (XPS, ESCALAB 250Xi). The specific surface area and pore size distribution of the samples were measured via a Brunner–Emmett–Teller (BET, BSD-PS) instrument and the Barret–Joyner–Halenda (BJH) model. The magnetic properties were measured by a physical property measurement system (PPMS, Dynacool-14T). The toroidal samples with inner and outer diameters of 3.04 mm and 7.00 mm were made according to the sample-to-paraffin mass ratio of 1 : 9. The complex permittivity and permeability of the composites were tested by a vector network analyzer (VNA; Agilent N5230A) at 2.0–18.0 GHz. The reflection loss (RL) values can be calculated according to the transmission line theory (Eqs. (1) and (2)) [53–55]:

$$\mathrm{RL}\,(\mathrm{dB}) = 20\log\left|\frac{Z_{\mathrm{in}}-Z_0}{Z_{\mathrm{in}}+Z_0}\right| \tag{1}$$

$$Z_{\mathrm{in}} = Z_0\sqrt{\frac{\mu_{\mathrm{r}}}{\varepsilon_{\mathrm{r}}}}\tanh\left(\mathrm{j}\frac{2\pi fd}{c}\sqrt{\mu_{\mathrm{r}}\varepsilon_{\mathrm{r}}}\right) \tag{2}$$

where Z_{in} and Z_0 are the input impedance of the absorber and free space, respectively; d and c are the thickness of the sample and the speed of light in vacuum, respectively; f is the frequency of EMW.

2.4 Calculation details

The density of states (DOS) and charge density difference of Fe/RGO were determined via the Cambridge serial total energy package (CASTEP) module in the Material Studio software. The generalized gradient approximation (GGA) Perdew–Burke–Ernzerhof (PBE) function was used as the exchange correlation function. The cutoff energy and k-point were set as 800 eV and 4 × 4 × 1, respectively. The convergence threshold was 10^{-5} eV in energy and 0.03 eV/Å in force. The thick vacuum region was set to be approximately 15 Å to prevent any fake interaction along the Z-axis.

The RCS simulation was performed with the CST Studio Suite software to evaluate the electromagnetic energy attenuation capability. Based on the metal back model, the constructed model with a 200 mm × 200 mm square consists of an upper absorbing layer (3.47 mm) and a bottom perfect electric conductor layer (PEC, 1.0 mm). The model was placed on the XOZ plane, and the incident direction of the EMW was along the negative direction of the Y-axis. The frequency was 8.48 GHz. The scattering directions of RCS value (σ) were determined by *theta* and *phi* in spherical coordinates in the model as Eq. (3) [56]:

$$\sigma\,(\mathrm{dB}m^2) = 10\log\left(\frac{4\pi S}{\lambda^2}\left|\frac{E_{\mathrm{s}}}{E_{\mathrm{i}}}\right|^2\right) \tag{3}$$

where S is the area of the simulated plate; λ is the wavelength of the EMW; E_{s} and E_{i} are the electric field intensities of the scattered wave and incident wave, respectively.

3 Results and discussion

3.1 Characterizations of Fe/RGO composites

According to transmission line theory, the real (ε') and imaginary (ε'') parts of the ideal ε_{r} of the EMWA material (RL ≤ −10 dB) were obtained at a specific thickness in this work. If ε_{r} meets the range of this region, electromagnetic energy absorption over a wide frequency range (2–18 GHz) can be realized. Figures 1(a)–1(c) shows the relationship between permittivity (ε' and ε'') and frequency at a given permeability (μ' = 1, μ'' = 0; μ' = 1.1, μ'' = 0.1; μ'' = 1.2, μ''= 0.2). Notably, ε' and ε'' gradually decrease with increasing frequency, which has a significant dielectric dispersion effect. Moreover, with increasing permeability, the variation ranges of the permittivity are gradually reduced due to the dielectric–magnetic loss mechanism, which provides theoretical guidance for us to quickly realize broadband EMWA. However, the shortcomings of pure graphene absorbers, such as their large permittivity and lack of magnetic loss, limit their EMWA performance. Therefore, how to control the introduction of magnetic materials to achieve the optimal regulation of graphene electromagnetic parameters is an important challenge. The Fe/RGO composites were prepared by simple hydrothermal and thermal reduction methods, as shown in Fig. 1(d). The microstructures of Fe/RGO composites were investigated by controlling the content of Fe particles. As shown in Fig. 1(e), Fe presents a regular and anisotropic hexagonal micron-sized sheet structure (~2 μm). With increasing Fe content, the irregular nanoparticles gradually form stable microsheets in Fe/RGO, and the Fe microsheets are uniformly dispersed on the RGO lamella (Fig. 1(f) and Fig. S1 in the Electronic Supplementary Material (ESM)). The microstructure of Fe/RGO 4 : 1 composite was further analyzed by TEM. Figures 1(g) and 1(h) show that the lattice fringe distance is 0.2 nm, corresponding to the (110) face of Fe. In addition, ordered diffraction spots can be observed in the selected area electron diffraction (SAED) pattern, indicating that Fe has a single-crystal structure. The element mapping images clearly show the uniform distribution of C, Fe, and O elements in the prepared Fe/RGO composite (Fig. 1(i)).

The phase and crystal structure were studied by XRD, as shown in Fig. 2(a). The Fe/RGO composites show a wide peak at approximately 25.8°, corresponding to the (002) plane, indicating that GO was successfully reduced to RGO [57]. The diffraction peaks at 44.73°, 65.04° and 82.38° correspond to the (110), (200), and (221) crystal faces of body-centered cubic (bcc) iron (PDF#06-0696) [58]. Obviously, with increasing Fe content, the diffraction peak intensity of Fe gradually increases. Furthermore, the Fe content in Fe/RGO was confirmed by ICP-MS, and the percentages are 8.75, 10.48, 24.16, 32.96, 57.62, 68.23, and 75.5 wt% in Fe/RGO (1 : 8, 1 : 4, 1 : 2, 1 : 1, 2 : 1, 4 : 1, and 8 : 1, respectively) (Fig. 2(b)). The degree of graphitization of Fe/RGO composites was assessed by Raman spectroscopy, where the D and G bands represent defects and graphitized carbon, respectively [59]. As shown in Fig. 2(c), the $I_{\mathrm{D}}/I_{\mathrm{G}}$ value increases with increasing Fe content (from 0.89 to 1.12), indicating that the introduction of Fe leads to more defects in RGO, which can act as dipoles to increase dipole polarization. The valence state and elemental composition of Fe/RGO composites were determined by XPS. The full spectrum shows that there are C, O and Fe elements in the Fe/RGO composite (Fig. 2(d)), which is consistent with the XRD results above. The high-resolution C 1s spectrum shows that the three peaks at 284.8, 285.5, and 288.4 eV correspond to the C=C, C–O, and O–C=O bonds, respectively (Fig. 2(e)). These functional groups can induce dipole polarization to optimize EMWA performance. The Fe 2p spectrum of Fe/RGO composite was further analyzed (Fig. 2(f)). The two peaks are Fe $2p_{3/2}$ and Fe $2p_{1/2}$ at 711.3 and 724.9 eV, which can be decomposed into Fe^{2+} $2p_{3/2}$ (711.2 eV), Fe^{3+} $2p_{3/2}$ (713.4 eV), Fe^{2+} $2p_{1/2}$ (724.8 eV), and $Fe^{3+}2p_{1/2}$ (727.0 eV). The results reveal

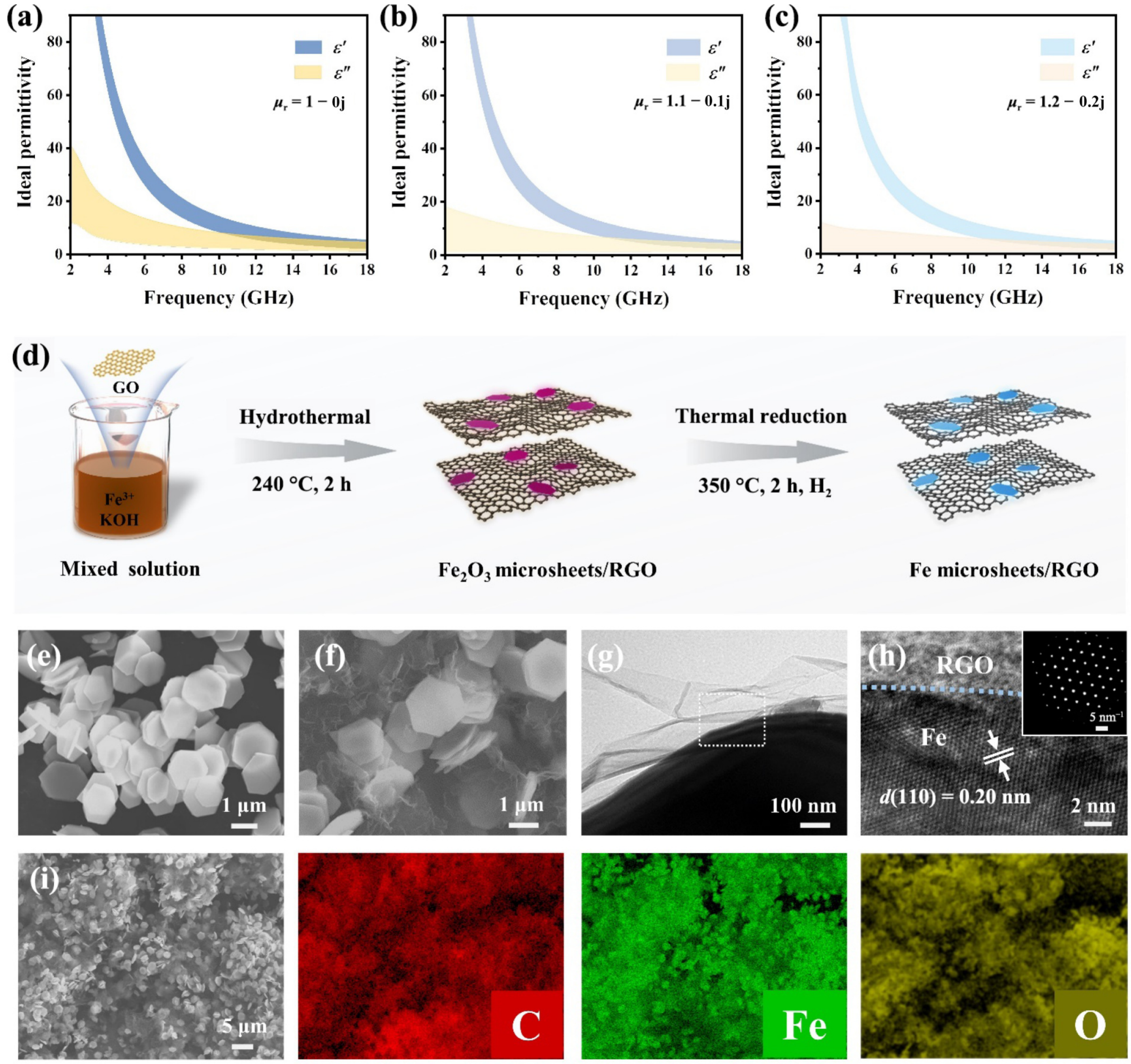

Fig. 1 (a–c) Ideal distribution region of real and imaginary parts of the permittivity at 2.40 mm for EMA materials. (d) Schematic diagram of synthesis process of Fe/RGO composite. (e, f) SEM images of Fe and Fe/RGO 4 : 1. (g, h) TEM and HRTEM images of Fe/RGO 4 : 1 (inset: SAED image). (i) SEM image and corresponding element mapping images of Fe/RGO 4 : 1.

the presence of Fe^{2+} and Fe^{3+} in the sample, which is attributed to the oxidation of the Fe surface during the test. The peak assignment to metal Fe^0 at 708.0 eV indicates that the Fe/RGO composites were successfully prepared. The specific surface area and pore size structure of Fe/RGO (1 : 1, 2 : 1, and 4 : 1) composites were studied by BET. As shown in Fig. 2(g), the adsorption and desorption curves of the three samples all present type IV isotherms, indicating that the samples exhibit mesoporous characteristics. The specific surface areas of Fe/RGO 1 : 1, Fe/RGO 1 : 2, and Fe/RGO 1 : 4 are 87.16, 72.85, and 60.76 $m^2 \cdot g^{-1}$, respectively, and the average pore sizes are 19.11, 19.45, and 22.14 nm, respectively. The above results show that the Fe content can affect the graphene conductive network structure and thus play a role in regulating its conductivity. Moreover, a large pore structure increases the propagation path of the EMW, which is conducive to impedance matching and multiple scattering, thus enhancing the attenuation ability. The magnetic properties of Fe/RGO composites were tested by PPMS, as shown in Figs. 2(h) and 2(i). The magnetic hysteresis loops of the samples have a typical S shape, showing an obvious ferromagnetic behavior. The saturation magnetization (M_s) of Fe is 125.12 $emu \cdot g^{-1}$. The decrease in M_s value of Fe/RGO composites can be attributed to the addition of non-magnetic RGO. With increasing Fe content, the M_s values gradually increases, indicating that the magnetic properties are improved. The M_s values of Fe/RGO 1 : 8, 1 : 4, 1 : 2, 1 : 1, 2 : 1, 4 : 1, and 8 : 1 are 13.89, 22.54, 30.69, 44.81, 56.17, 77.39, and 91.50 $emu \cdot g^{-1}$, respectively, and the coercivities are 0.37, 0.39, 0.35, 0.31, 0.36, 0.28, and 0.29 kOe, respectively. High M_s and low coercivity (H_c) can be conducive to magnetic loss, thereby improving the EMWA performance.

3.2 Analysis of electromagnetic parameters and EMWA performance

To understand the influence of the ratio of RGO and Fe on EMWA performance, the electromagnetic parameters ($\varepsilon_r = \varepsilon' - j\varepsilon''$, and $\mu_r = \mu' - j\mu''$) of Fe/RGO composites were analyzed at 2–18 GHz, as shown in Figs. 3(a)–3(d). The ideal permittivity values obtained in Figs. 1(a)–1(c) were statistically compared. With increasing magnetic properties, the ε' and ε'' gradually decrease. Figures 3(a) and 3(b) show that the variation trends of ε'

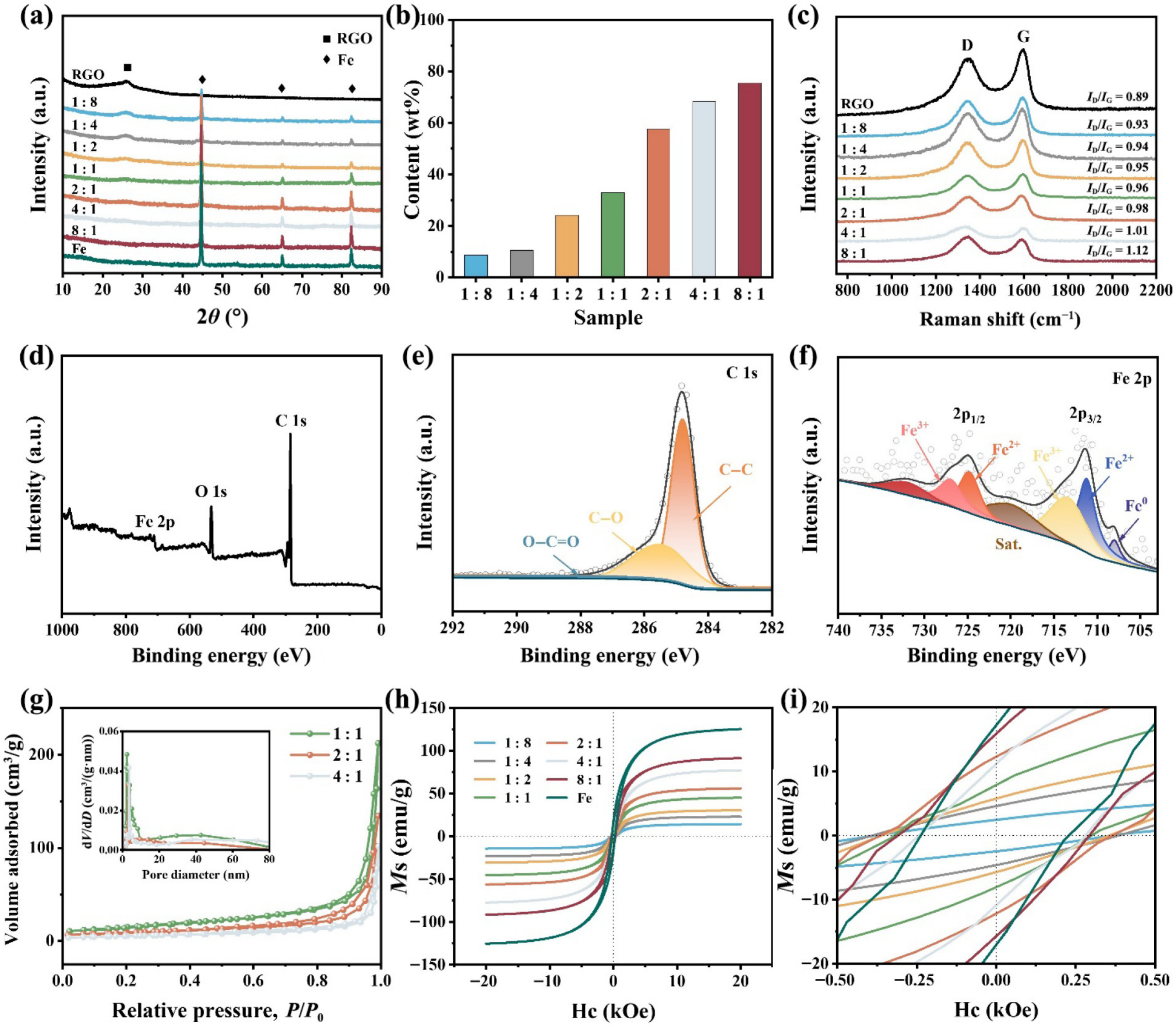

Fig. 2 (a) XRD patterns, (b) Fe content inICP measurement, (c) Raman spectra of materials. (d) XPS spectra and (e) C 1s and (f) Fe 2p spectra of Fe/RGO 4 : 1. (g) N_2 adsorption/desorption isotherms and pore size distribution plots. (h, i) Magnetic hysteresis loops of materials.

and ε'' of the real measurement are very similar to the ideal ε_r. ε_r of samples slowly decreases with increasing frequency, which can be attributed to the dielectric dispersion behavior due to the hysteresis effect of polarization changing with the electric field. In addition, with increasing Fe content, ε' is distributed only in the ideal region in the middle- and high-frequency ranges, whereas ε'' can be widely dispersed in the ideal region. Pure RGO has high ε' (10.78–28.10) and ε'' (10.14–39.90) values due to its conductive network and rich interface structure, but the EMWA performance is weak due to impedance mismatch (Fig. S2(a) in the ESM). The Fe microsheets have low ε' values (3.90–4.33) and ε'' values (0–0.32) and poor EMWA properties due to their high density (Fig. S2(d) in the ESM). Notably, the ε' and ε'' values of the samples decrease with increasing Fe content, indicating that the Fe microsheets have an important effect on the regulation of the dielectric properties of graphene. This is because the Fe microsheets anchored to the RGO lamella hinder the formation of the graphene conductive network structure, resulting in decreased dielectric properties. In detail, the ε' and ε'' values of Fe/RGO 1 : 8 decrease from 19.02 to 9.71 and from 15.78 to 6.07, respectively. For Fe/RGO 1 : 4, the ε' value decreases from 18.23 to 7.79, and the ε'' value decreases from 10.14 to 4.45. The ε' and ε'' values of Fe/RGO 1 : 2 decrease from 14.03 to 7.61 and from 5.90 to 3.45, respectively. For Fe/RGO 1 : 1, the ε' value decreases from 12.21 to 7.04, and the ε'' value decreases from 4.17 to 2.61. The ε' and ε'' values of Fe/RGO 2 : 1 decrease from 10.54 to 5.91 and from 3.61 to 2.44, respectively. The ε' and ε'' values of Fe/RGO 4 : 1 decrease from 9.15 to 5.15 and from 3.17 to 2.12, respectively. The ε' and ε'' values of Fe/RGO 8 : 1 decrease from 6.83 to 4.37 and from 1.56 to 1.37, respectively. In addition, the samples show resonant peaks at 10–14 and 14–18 GHz, which are attributed to multi-polarization relaxation. As shown in Figs. 3(c) and 3(d), the μ' and μ'' values increase with increasing Fe content. Among them, Fe microheets have high μ' and μ'' values (1–1.18, 0.1–0.19). Notably, the samples exhibit multiple resonant peaks at 2–18 GHz, mainly due to resonance and eddy current effects. The EMWA performance was evaluated according to transmission line theory using electromagnetic parameters. Figures 3(e)–3(n) and Fig. S2 in the ESM show the RL variation curves with frequency and thickness. For Fe/RGO 1 : 2 (Figs. 3(e) and 3(i)), the RL_{min} value is −29.4 dB at 2.37 mm, and the EAB_{max} is 5.97 GHz (12.03–18 GHz) at 1.89 mm. As the Fe content increases, Fe/RGO 1 : 1 shows RL_{min} of −54.58 dB at 5.76 GHz (4.44 mm) and EAB_{max} of 6.02 GHz (10.92–16.94 GHz) at 2.07 mm (Figs. 3(f) and 3(j)). Fe/RGO 2 : 1 exhibits RL_{min} of −56.69 dB at 11.12 GHz (2.75 mm) and EAB_{max} of 6.86 GHz (11.14–18 GHz) at

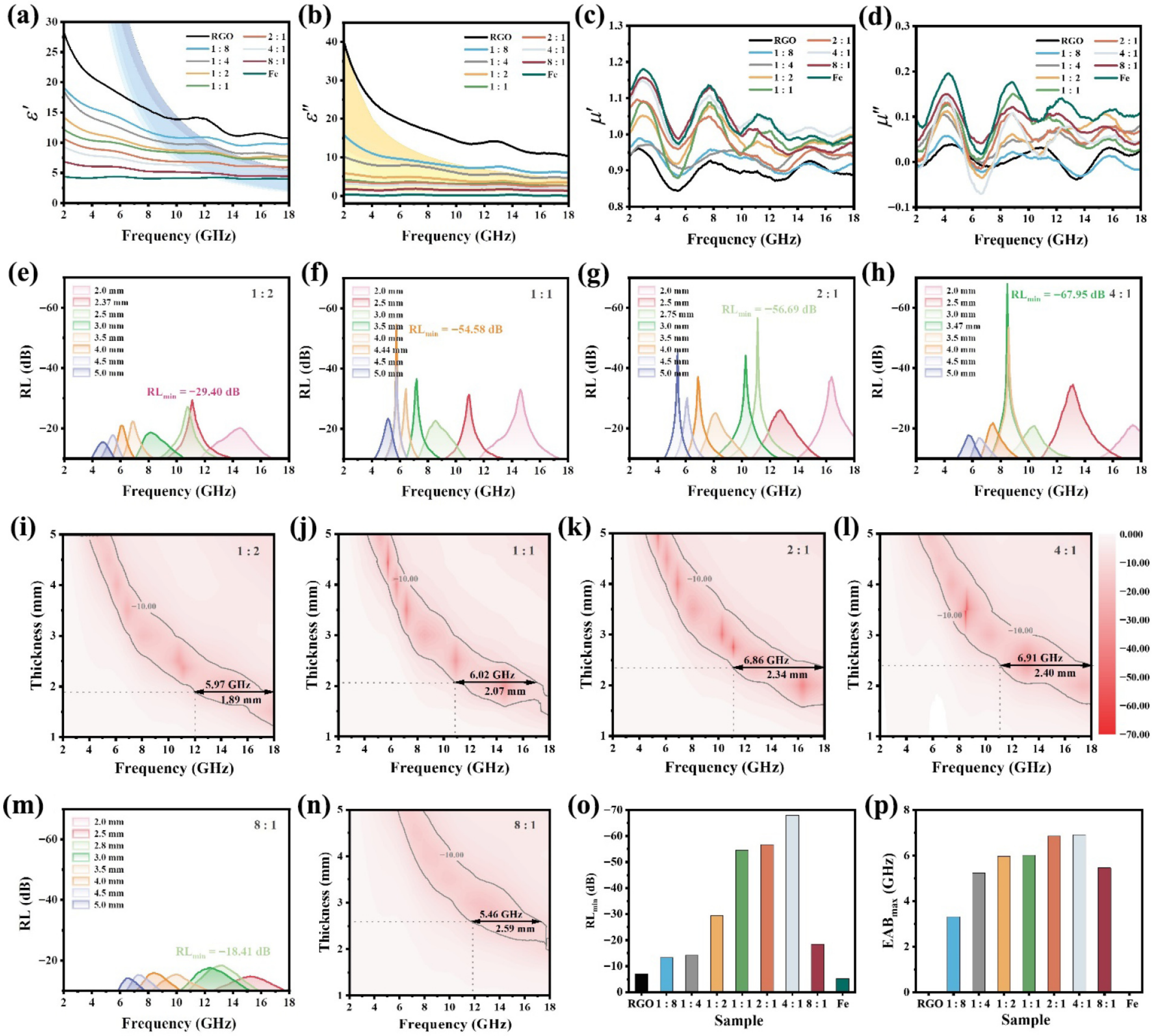

Fig. 3 (a) ε', (b) ε'', (c) μ', and (d) μ'' of all samples. (e–n) 2D RL contour plots and RL values with different thicknesses and frequencies of Fe/RGO 1 : 2, 1 : 1, 2 : 1, 4 : 1, and 8 : 1. (o, p) Summarization of RL_{min} and EAB_{max} of samples.

2.34 mm (Figs. 3(g) and 3(k)). With a further increase in the Fe content, Fe/RGO 4 : 1 achieves the best EMWA performance, showing better performance than the other samples. The RL_{min} value is −67.95 dB at 8.48 GHz (3.47 mm), and the EAB_{max} is 6.91 GHz (11.09–18 GHz) at 2.40 mm. For Fe/RGO 1 : 8, Fe/RGO 1 : 4, and Fe/RGO 8 : 1, the EMWA performance is relatively weak. The high conductivity of RGO causes strong reflections between the air and material interfaces due to impedance mismatch, which limits the improvement in EMWA performance. However, when the amount of Fe is excessive, the conductive network structure cannot be formed, resulting in a decrease in the dielectric loss capacity. These results indicate that the excellent EMWA properties of Fe/RGO composites can be effectively regulated by changing the contents of RGO and Fe. RL_{min} and EAB_{max} of the samples are visually summarized to evaluate EMWA performance (Figs. 3(o) and 3(p)). The Fe/RGO 4 : 1 composite exhibits high loss and wide-band EMWA performance, which is attributed to the dielectric–magnetic loss mechanism of RGO and Fe.

3.3 Analysis of EMWA performance and mechanism

To further elucidate the mechanism of electromagnetic loss, the attenuation mechanisms of dielectric loss (conduction and polarization) and magnetic loss (resonance and eddy current) are analyzed. Figure 4(a) shows that $\tan\delta_\varepsilon$ increases with increasing RGO loading, indicating increased dielectric loss. Notably, the sample exhibits a resonant peak at 11.12–15.81 GHz, which is attributed to the multi-polarization relaxation behavior. Based on Debye theory, the polarization loss (ε_p'') and conductance loss (ε_c'') can be expressed as Eqs. (4) and (5) [60–63]:

$$\varepsilon' = \varepsilon_\infty + \frac{\varepsilon_s - \varepsilon_\infty}{1 + \omega^2\tau^2} \tag{4}$$

$$\varepsilon'' = \varepsilon_p'' + \varepsilon_c'' = \frac{\varepsilon_s - \varepsilon_\infty}{1 + \omega^2\tau^2}\omega\tau + \frac{\sigma}{\omega\varepsilon_0} \tag{5}$$

where ω represents the angular frequency; τ is the polarization relaxation time, ε_s is the static permittivity and ε_∞ is the relative permittivity at high frequency. To explore the relationship between conductance and polarization losses, the contributions of ε_c'' and ε_p'' are obtained by fitting the relaxation model, as shown in Figs. 4(b)–4(d) and Fig. S3 in the ESM. The conduction loss is dominant at low frequencies, while the polarization loss is dominant at high frequencies. Moreover, Fig. 4(c) shows that the average $\varepsilon_p''/\varepsilon_c''$ values of all samples are higher than 1, which indicates that polarization loss is the dominant form of dielectric

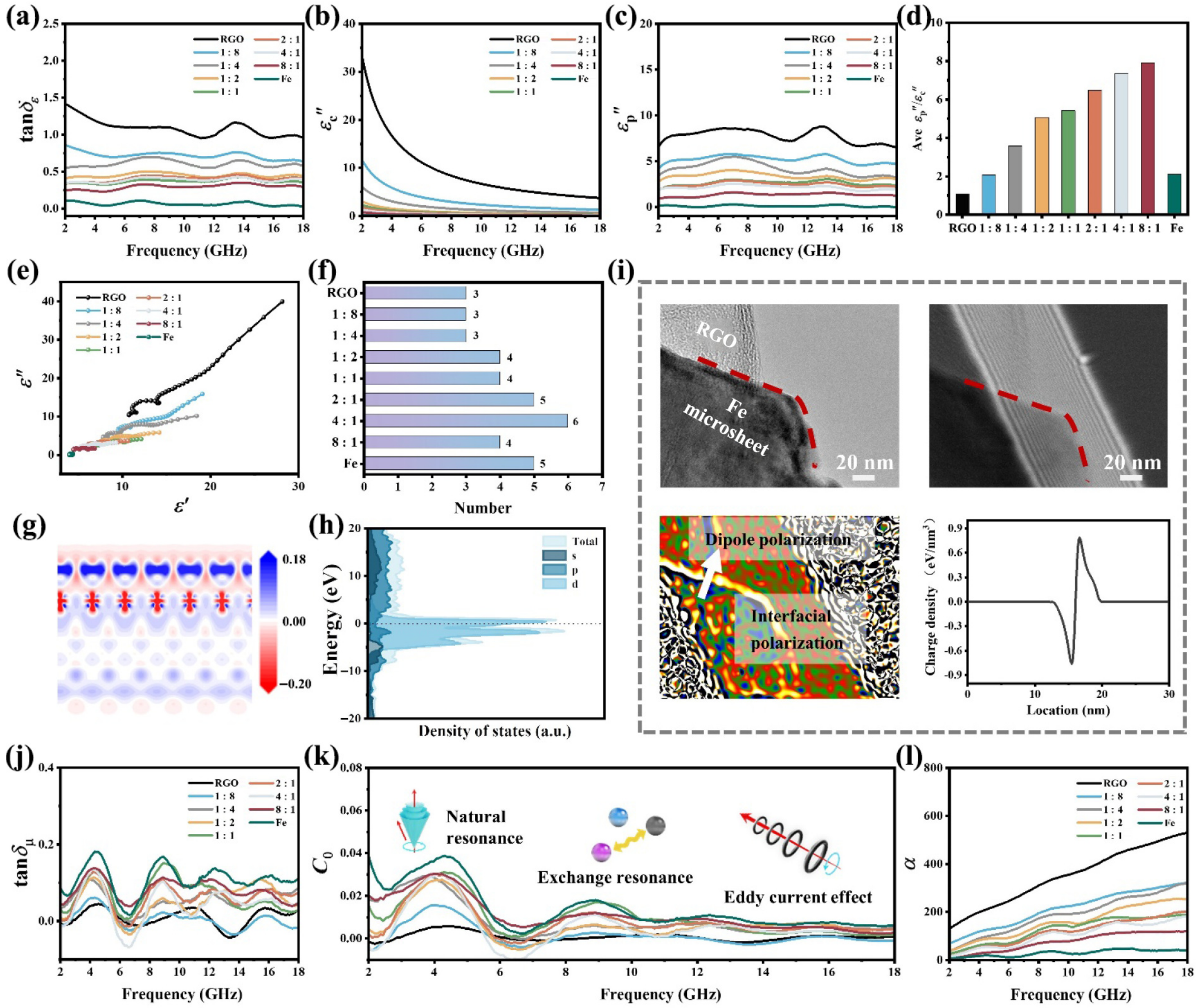

Fig. 4 (a) tanδ_ε, (b) ε_c'', (c) ε_p'', (d) average $\varepsilon_p''/\varepsilon_c''$, (e) Cole–Cole curves, and (f) $\varepsilon'' - \varepsilon'$ semicircular number of samples. (g) Charge density difference of Fe/graphene and (h) ε_r results. (i) TEM image and off-axis electron hologram, charge density distribution diagram, and white arrow charge density curve of Fe/RGO 4 : 1. (j) tanδ_μ, (k) C_0, and (l) attenuation constant of samples.

loss. The dielectric loss mechanism of the absorber was analyzed using Debye theory (Cole–Cole model) [64–66]. The semicircular curve is related to the polarization loss, and the straight line is related to the conduction loss. [67]. Figures 4(e) and 4(f) and Fig. S5 in the ESM show the Cole–Cole curves for all the samples. Multiple semicircles can clearly be observed, which indicates the existence of multiple polarization relaxation processes in Fe/RGO composites, such as dipole polarization and interface polarization. The smooth tail indicates that Fe and RGO are interconnected to form a conductive network which enhances conductive losses at low frequencies. The residual functional groups of RGO and the defects caused by the introduction of metallic Fe form the polarization center, thus inducing dipole polarization. In addition, the rich heterogeneous interface between metallic Fe microsheets and RGO leads to interfacial polarization. To better understand the interfacial polarization loss mechanism, a Fe(110)/graphene(001) two-dimensional heterogeneous interface structure (Fig. S6 in the ESM) was constructed. The charge density difference and DOS were calculated using DFT to analyze the electronic interaction between Fe and graphene interfaces, as shown in Figs. 4(g) and 4(h). Charge transfer occurs between the Fe and graphene because the difference in the Fermi energy levels results in an uneven distribution of electrons between the heterogeneous interfaces (blue and red areas indicate electron accumulation and electron depletion). In addition, the density of states of Fe/graphene indicates that the migration of electrons from Fe atoms to C atoms results in a rearrangement of electrons due to hybridization of 3d–2p orbitals at the Fermi level, thus enhancing interfacial polarization. The interfacial polarization of Fe/RGO was verified by off-axis electron hologram technology, as shown in Fig. 4(i). The charge density distribution diagram shows that the positive and negative charges are distributed in the interfacial contact area between the Fe microsheets and the RGO layer, forming a built-in electric field. Unbalanced charge accumulation can induce interfacial polarization at heterogeneous interfaces. Under the action of an electromagnetic field, the electric dipole turns repeatedly to promote interface polarization, thereby consuming the EMW energy. Moreover, it also has an uneven charge distribution phenomenon inside the graphene laminates, which indicates that defects in its interior induce dipole polarization to increase dielectric loss. Furthermore, magnetic loss (eddy current loss, natural resonance, and exchange resonance) is also an important part of EMW energy attenuation. Figure 4(j) shows that tanδ_μ tends to increase with increasing Fe load, which indicates that the magnetic loss is increased. The contribution of eddy current loss to magnetic loss is generally defined as $C_0 = \mu''(\mu')^{-2}f^{-1}$ [68,69]. When the magnetic loss comes only from the eddy current loss, the C_0 value is a constant. When the C_0 value significantly fluctuates, the magnetic loss mainly arises from the natural resonance and the exchange resonance. As shown in Fig. 4(k), the magnetic loss of samples is derived from natural resonance (2.56–6.64 GHz), exchange resonance (6.64–10.84 GHz) and eddy current effects (10.84–18 GHz). Therefore, the above-mentioned dielectric–magnetic loss mechanism jointly attenuates the EMW energy. To clearly demonstrate the regulatory effects of Fe on graphene, the dielectric properties of the RGO composite were investigated based on the above ratio of pure RGO in Fe/RGO 4 : 1 (Fig. 2(b) and Fig. S7 in the ESM). As shown in Figs. S7(a) and S7(b) in the ESM, compared with Fe/RGO 4 : 1, RGO' has lower ε_r, and ε_r is distributed outside the ideal complex permittivity region ($\mu' = 1$, $\mu'' = 0$), which indicates weak EMWA performance. In addition, Fe microsheets greatly improve the polarization loss of graphene (Figs. S7(c) and S7(d) in the ESM). The above results show that the interaction between Fe and RGO not only optimizes ε_r of graphene but also contributes to the magnetic loss, thus resulting in excellent EMWA performance. In general, the attenuation constant (α) is used to evaluate the energy attenuation ability of the absorbing material (Eq. (6)) [70–72]:

$$\alpha = \frac{\sqrt{2}\pi f}{c} \times \sqrt{(\mu''\varepsilon'' - \mu'\varepsilon') + \sqrt{(\mu''\varepsilon'' - \mu'\varepsilon')^2 + (\varepsilon'\mu'' + \varepsilon''\mu')^2}} \quad (6)$$

Figure 4(l) shows that the α values decrease with increasing Fe

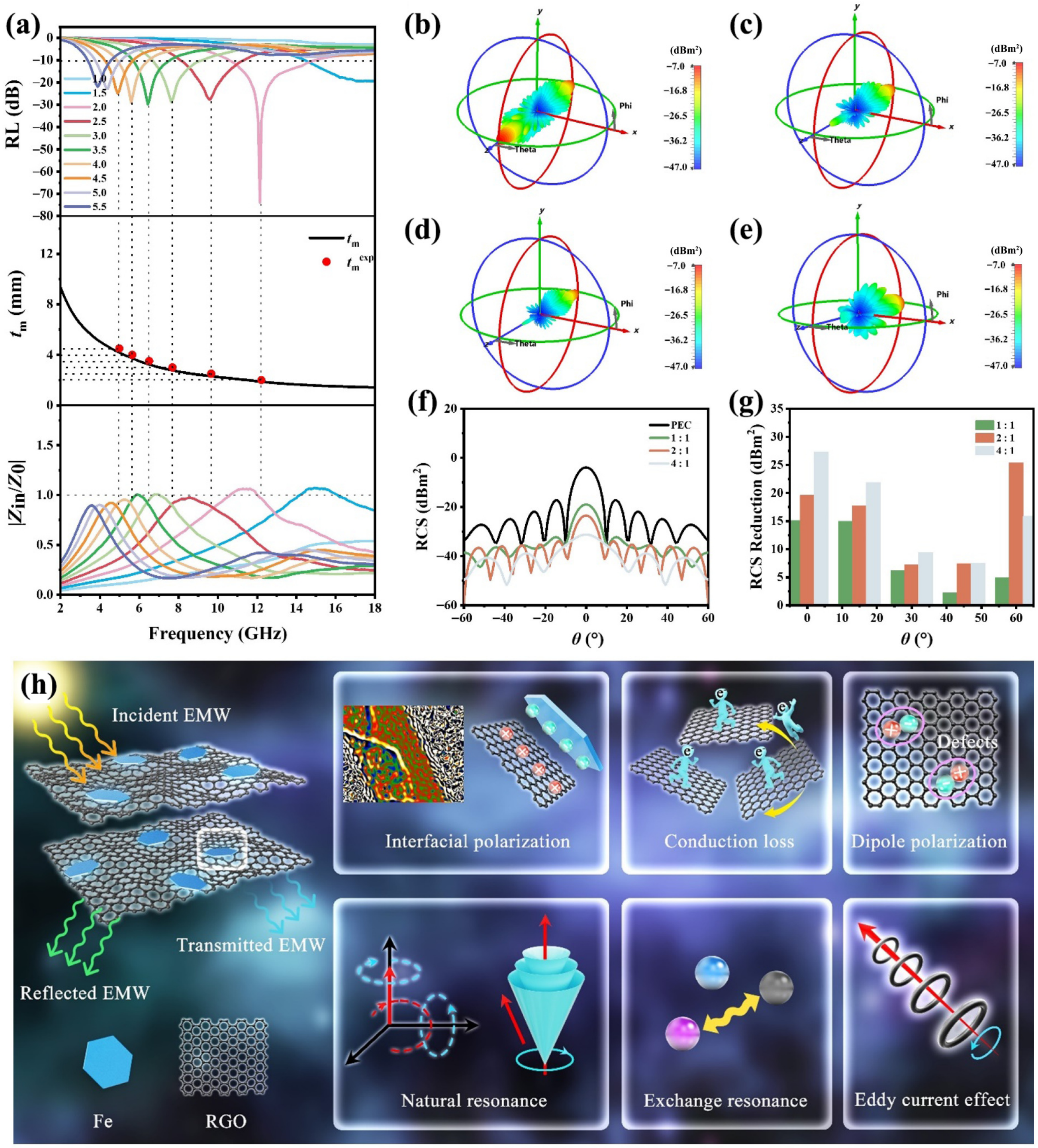

Fig. 5 (a) RL values and simulated and experimental values of matching thicknesses under $\lambda/4$ condition, and impedance matching values for Fe/RGO 4 : 1. CST simulation results of (b) PEC, (c) Fe/RGO 1 : 1, (d) Fe/RGO 2 : 1, and (e) Fe/RGO 4 : 1. (f) RCS simulation curves. (g) RCS reduction values. (h) Schematic diagram of EMWA mechanism of Fe/RGO.

content and increase with increasing frequency. Obviously, RGO has a high α value, but the EMWA performance is poor due to impedance mismatch (Fig. S4 in the ESM). The closer the Z value of the absorbing material is to 1, the better the impedance match is, indicating that more electromagnetic waves enter the material and thus increase the energy consumption [73–75]. The large surface area and network structure of Fe/RGO produce multiple reflections and scattering, resulting in more EMWA. Therefore, only appropriate attenuation characteristics and impedance matching can achieve excellent EMWA performance.

The relationship between the thickness and absorption peak frequency of the absorbers can be explained by a quarter-wavelength (λ/4) model [76]. In this model, the RL_{min} peaks shift to low frequencies with increasing thickness (Eq. (7)) [77–79]:

$$t_m = \frac{n}{4}\lambda = \frac{nc}{4f_m\sqrt{|\mu_r\varepsilon_r|}} \quad (n = 1, 3, 5, \cdots) \tag{7}$$

where t_m and f_m represent the matching thickness and the frequency, respectively. As shown in Fig. 5(a), the RL_{min}, thickness, and theoretical λ/4 curve of Fe/RGO 4 : 1 composite are consistent with the impedance matching values. The strong EMWA performance of Fe/RGO 4 : 1 conforms to the interference cancellation law of a quarter wavelength, resulting in intense attenuation of EMW energy. To simulate the EMW stealth performance of Fe/RGO in a real environment, RCS simulation of samples was carried out by CST software. Figures 5(b)–5(e) show the RCS simulation results of PEC, Fe/RGO 1 : 1, Fe/RGO 2 : 1, and Fe/RGO 4 : 1. Obviously, all the samples clearly have similar shapes but different intensities in the 3D radar wave scattering signal. Figure 5(f) shows the RCS curves from −60° to 60°. The scattered signal is the strongest when the detection angle is 0°. Compared with the high RCS value of PEC (−3.87 dBm^2), Fe/RGO composites can significantly reduce the scattered signal of radar waves, and the Fe/RGO ratio of 4 : 1 results in an excellent RCS suppression signal (−31.21 dBm^2). To compare the EMW dissipation ability of different samples, the RCS values of five specific detection angles (0°, 15°, 30°, 45°, and 60°) are obtained by reducing the RCS values of the PEC layer. As shown in Fig. 5(g), Fe/RGO samples can inhibit radar wave reflection to a certain extent. Among them, Fe/RGO 4 : 1 shows the best RCS inhibition (from 4.93 to 27.34 dBm^2). Therefore, the above results show that Fe/RGO 4 : 1 has excellent EMWA performance and broad practical application prospects. Based on the above experimental and simulation results, the EMWA mechanisms of Fe/RGO composites were analyzed, as shown in Fig. 5(h). First, the unique 3D structure of RGO is beneficial to extending the propagation path of electromagnetic waves, leading to multiple reflections and scattering, thus promoting the multiple attenuation of EMW energy. Second, the heterogeneous interfaces between the Fe microsheets and RGO sheets can cause strong interfacial polarization and thus increase the dielectric loss. Third, the continuous conductive network structure between RGO lamellae is conducive to electron migration and jumping, thus enhancing conduction loss. Fourth, the abundant defects and polar functional groups in the Fe/RGO composite can be used as polarization centers to induce dipole polarization. Finally, the magnetic loss caused by natural and exchange resonances and eddy current losses of Fe further consume the EMW energy. Therefore, Fe/RGO exhibits significant EMWA performance through the dielectric–magnetic loss mechanism.

4 Conclusions

In summary, a series of Fe/RGO composites with 3D structures were successfully prepared by hydrothermal and thermal reduction strategies. The complex permittivity and permeability of Fe/RGO composites were regulated by controlling the mass ratio of Fe to RGO. The introduction of anisotropic Fe microsheets reduces the conductivity and dielectric parameters of RGO, which helps to improve impedance matching and reduce the matching thickness of absorbers. RL_{min} of Fe/RGO 4 : 1 reaches −67.95 dB at 8.48 GHz (3.47 mm), and EAB_{max} reaches 6.91 GHz (11.09–18 GHz) at 2.40 mm. The excellent EMWA performance is attributed to the dielectric–magnetic loss mechanisms of RGO and Fe, including multiple reflections and scattering, interface polarization, dipole polarization, conduction loss, natural resonance, exchange resonance, and eddy current loss. In addition, Fe/RGO demonstrates excellent radar stealth performance through CST simulation under far-field conditions, and the RCS value reaches −31.21 dBm^2 at 0°. Therefore, this study is expected to provide valuable ideas for the design and development of lightweight and efficient EMWA materials.

Acknowledgements

This work was supported by the National Natural Science Foundation of China (Nos. 52432002, 52372041, and 52302087), the Heilongjiang Touyan Team Program, the Fundamental Research Funds for the Central Universities (No. HIT.OCEF.2021003), and the Shanghai Aerospace Science and Technology Innovation Fund (No. SAST2022-60).

Declaration of competing interest

The authors have no competing interests to declare that are relevant to the content of this article. The author Dechang Jia is the Editorial Committee member of this journal.

Electronic Supplementary Material

Supplementary material is available in the online version of this article at https://doi.org/10.26599/JAC.2024.9220990.

References

[1] Xue TT, Yang Y, Yu DY, *et al.* 3D printed integrated gradient-conductive MXene/CNT/polyimide aerogel frames for electromagnetic interference shielding with ultra-low reflection. *Nano-Micro Lett* 2023, **15**: 45.

[2] Tao JQ, Zhou JT, Yao ZJ, *et al.* Multi-field coupled motion induces electromagnetic wave absorbing property regeneration of elastomer in marine environment. *Adv Funct Mater* 2024, **34**: 2310640.

[3] Wang L, Cai ZX, Su L, *et al.* Bifunctional SiC/Si_3N_4 aerogel for highly efficient electromagnetic wave absorption and thermal insulation. *J Adv Ceram* 2023, **12**: 309–320.

[4] Yan YF, Zhang KL, Qin GY, *et al.* Phase engineering on MoS_2 to realize dielectric gene engineering for enhancing microwave absorbing performance. *Adv Funct Mater* 2024, **34**: 2316338.

[5] Qiao LJ, Bi JQ, Liang GD, *et al.* Synthesis of high-entropy MXenes with high-efficiency electromagnetic wave absorption. *J Adv Ceram* 2023, **12**: 1902–1918.

[6] Qiu JF, Liu X, Peng CY, *et al.* Porous metal microsphere M@C–rGO (metal = Mn, Fe, Co, Ni, Cu) aerogels with high low-frequency microwave absorption, strong thermal insulation and superior anticorrosion performance. *J Mater Chem A* 2024, **12**: 21997–22012.

[7] Guo KY, Chen L, Yang GJ. Boosting electromagnetic wave absorption of Ti_3AlC_2 by improving effective electrical conductivity. *J Adv Ceram* 2023, **12**: 1533–1546.

[8] Wang ZJ, Zhang F, Wang NN, *et al.* Ternary layered boride MoAlB: A novel thermo-regulation microwave absorbing ceramic material. *J Adv Ceram* 2024, **13**: 699–710.

[9] Liang WH, Wu JT, Zhang S, *et al.* Porous $Ti_3C_2T_x$ MXene nanosheets

sandwiched between polyimide fiber mats for electromagnetic interference shielding. *Nano Res* 2024, **17**: 2070–2078.
[10] Cao MS, Wang XX, Zhang M, *et al.* Electromagnetic response and energy conversion for functions and devices in low-dimensional materials. *Adv Funct Mater* 2019, **29**: 1807398.
[11] Zhang S, Wu JT, Liang WH, *et al.* Flexible and multifunctional polyimide-based composite films by self-reducing reaction for electromagnetic interference shielding in extreme environments. *Carbon* 2023, **212**: 118103.
[12] Liang WH, Wu JT, Zhang S, *et al.* Construction of PI–MXene–MWCNT nanocomposite film integrating conductive gradient with sandwich structure for high-efficiency electromagnetic interference shielding in extreme environments. *Carbon* 2024, **228**: 119328.
[13] He P, Zhou QQ, Wang H, *et al.* Hollow magnetic Fe_3O_4 nanospheres for excellent electromagnetic wave absorption. *Ceram Int* 2024, **50**: 4980–4986.
[14] Wang YP, Hui ZZ, Hao GZ, *et al.* Structural and component optimization of conventional magnetic material Co to synthesis dendritic-like FeCo and rose-like CoNi toward high-performance electromagnetic wave absorption. *J Mater Res Technol* 2022, **19**: 418–430.
[15] Zhou R, Wang YS, Liu ZY, *et al.* Digital light processing 3D-printed ceramic metamaterials for electromagnetic wave absorption. *Nano-Micro Lett* 2022, **14**: 122.
[16] Guo YQ, Ruan KP, Wang GS, *et al.* Advances and mechanisms in polymer composites toward thermal conduction and electromagnetic wave absorption. *Sci Bull* 2023, **68**: 1195–1212.
[17] Zhao TK, Hou CL, Zhang HY, *et al.* Electromagnetic wave absorbing properties of amorphous carbon nanotubes. *Sci Rep* 2014, **4**: 5619.
[18] Ye F, Song Q, Zhang ZC, *et al.* Direct growth of edge-rich graphene with tunable dielectric properties in porous Si_3N_4 ceramic for broadband high-performance microwave absorption. *Adv Funct Mater* 2018, **28**: 1707205.
[19] Liu YH, Huang XX, Yan X, *et al.* Pushing the limits of microwave absorption capability of carbon fiber in fabric design based on genetic algorithm. *J Adv Ceram* 2023, **12**: 329–340.
[20] Dai YW, Sun MQ, Liu CG, *et al.* Electromagnetic wave absorbing characteristics of carbon black cement-based composites. *Cement Concrete Comp* 2010, **32**: 508–513.
[21] Wu Y, Zhao Y, Zhou M, *et al.* Ultrabroad microwave absorption ability and infrared stealth property of nano-micro CuS@rGO lightweight aerogels. *Nano-Micro Lett* 2022, **14**: 171.
[22] Selseleh-Zakerin E, Mirkhan A, Shafiee M, *et al.* Plasma engineering toward improving the microwave-absorbing/shielding feature of a biomass-derived material. *Langmuir* 2024, **40**: 12148–12158.
[23] Fahimi A, Fakharian P, Mirakhan A, *et al.* Elemental doping and size effect-modified biomass-derived carbon: A fascinating microwave absorbing/shielding and energy saving material. *J Mater Chem C* 2024, **12**: 12535–12548.
[24] Peymanfar R, Moradi F. Functionalized carbon microfibers (biomass-derived) ornamented by Bi_2S_3 nanoparticles: An investigation on their microwave, magnetic, and optical characteristics. *Nanotechnology* 2021, **32**: 065201.
[25] Novoselov KS, Geim AK, Morozov SV, *et al.* Electric field effect in atomically thin carbon films. *Science* 2004, **306**: 666–669.
[26] Murali R, Yang YX, Brenner K, *et al.* Breakdown current density of graphene nanoribbons. *Appl Phys Lett* 2009, **94**: 243114.
[27] Li WX, Zhao WC, Cheng SB, *et al.* Terahertz selective active electromagnetic absorption film based on single-layer graphene. *Surf Interfaces* 2023, **40**: 103042.
[28] Tian YR, Zhi DD, Li T, *et al.* Graphene-based aerogel microspheres with annual ring-like structures for broadband electromagnetic attenuation. *Chem Eng J* 2023, **464**: 142644.
[29] Xia YX, Gao WW, Gao C. A review on graphene-based electromagnetic functional materials: Electromagnetic wave shielding and absorption. *Adv Funct Mater* 2022, **32**: 2204591.
[30] Xia XD, Wang Y, Zhong Z, *et al.* A theory of electrical conductivity, dielectric constant, and electromagnetic interference shielding for lightweight graphene composite foams. *J Appl Phys* 2016, **120**: 085102.
[31] Tan CL, Cao XH, Wu XJ, *et al.* Recent advances in ultrathin two-dimensional nanomaterials. *Chem Rev* 2017, **117**: 6225–6331.
[32] Yan SY, Shao SP, Tang YX, *et al.* Ultralight hierarchical Fe_3O_4/MoS_2/rGO/$Ti_3C_2T_x$ MXene composite aerogels for high-efficiency electromagnetic wave absorption. *ACS Appl Mater Inter* 2024, **16**: 36962–36972.
[33] Yao LH, Wang YC, Zhao JG, *et al.* Multifunctional nanocrystalline-assembled porous hierarchical material and device for integrating microwave absorption, electromagnetic interference shielding, and energy storage. *Small* 2023, **19**: 2208101.
[34] Cui C, Guo RH, Ren EH, *et al.* MXene-based rGO/Nb_2CT_x/Fe_3O_4 composite for high absorption of electromagnetic wave. *Chem Eng J* 2021, **405**: 126626.
[35] Zhao B, Li Y, Zeng QW, *et al.* Galvanic replacement reaction involving core–shell magnetic chains and orientation-tunable microwave absorption properties. *Small* 2020, **16**: 2003502.
[36] Yang BT, Fang JF, Xu CY, *et al.* One-dimensional magnetic FeCoNi alloy toward low-frequency electromagnetic wave absorption. *Nano-Micro Lett* 2022, **14**: 170.
[37] Wu HJ, Zhao ZH, Wu GL. Facile synthesis of FeCo layered double oxide/raspberry-like carbon microspheres with hierarchical structure for electromagnetic wave absorption. *J Colloid Interf Sci* 2020, **566**: 21–32.
[38] Liu XY, Zhou JM, Xue Y, *et al.* Structural engineering of hierarchical magnetic/carbon nanocomposites via *in situ* growth for high-efficient electromagnetic wave absorption. *Nano-Micro Lett* 2024, **16**: 174.
[39] Huang WH, Song M, Wang S, *et al.* Dual-step redox engineering of 2D CoNi-alloy embedded B, N-doped carbon layers toward tunable electromagnetic wave absorption and light-weight infrared stealth heat insulation devices. *Adv Mater* 2024, **36**: 2403322.
[40] Shu Y, Zhao TK, Li YT, *et al.* Porous Fe/FeO/Fe_2O_3 nanorod/RGO composites with high-efficiency electromagnetic wave absorption property. *Appl Surf Sci* 2023, **626**: 157223.
[41] Zheng W, Ye W, Yang P, *et al.* Recent progress in iron-based microwave absorbing composites: A review and prospective. *Molecules* 2022, **27**: 4117.
[42] Shi XF, You WB, Li X, *et al.* *In-situ* regrowth constructed magnetic coupling 1D/2D Fe assembly as broadband and high-efficient microwave absorber. *Chem Eng J* 2021, **415**: 128951.
[43] Zhang XF, Li YX, Liu RG, *et al.* High-magnetization FeCo nanochains with ultrathin interfacial gaps for broadband electromagnetic wave absorption at gigahertz. *ACS Appl Mater Inter* 2016, **8**: 3494–3498.
[44] Sun JC, He ZD, Dong WJ, *et al.* Broadband and strong microwave absorption of Fe/Fe_3C/C core–shell spherical chains enhanced by dual dielectric relaxation and dual magnetic resonances. *J Alloys Compd* 2019, **782**: 193–202.
[45] Zhang YB, Wang P, Wang Y, *et al.* Synthesis and excellent electromagnetic wave absorption properties of parallel aligned FeCo@C core–shell nanoflake composites. *J Mater Chem C* 2015, **3**: 10813–10818.
[46] Li YN, Guan ZJ, Jiang JT, *et al.* Evolution of the microstructure and electromagnetic properties of Fe–Si–Al particles during post ball-milling annealing. *J Mater Res Technol* 2024, **29**: 3532–3542.
[47] Cai B, Zhou L, Zhao PY, *et al.* Interface-induced dual-pinning mechanism enhances low-frequency electromagnetic wave loss. *Nat Commun* 2024, **15**: 3299.
[48] Zhang HB, Cheng JY, Wang HH, *et al.* Initiating VB-group laminated NbS_2 electromagnetic wave absorber toward superior absorption bandwidth as large as 6.48 GHz through phase engineering modulation. *Adv Funct Mater* 2022, **32**: 2108194.
[49] Wu ZC, Cheng HW, Jin C, *et al.* Dimensional design and core–shell

engineering of nanomaterials for electromagnetic wave absorption. *Adv Mater* 2022, **34**: 2107538.
[50] Peymanfar R, Fazlalizadeh F. Microwave absorption performance of $ZnAl_2O_4$. *Chem Eng J* 2020, **402**: 126089.
[51] Peymanfar R, Javanshir S, Naimi-Jamal MR, *et al.* Morphology and medium influence on microwave characteristics of nanostructures: A review. *J Mater Sci* 2021, **56**: 17457–17477.
[52] Zhang KL, Liu YH, Liu YN, *et al.* Tracking regulatory mechanism of trace Fe on graphene electromagnetic wave absorption. *Nano-Micro Lett* 2024, **16**: 66.
[53] Yang JC, Wen QB, Feng B, *et al.* Microstructural evolution and electromagnetic wave absorbing performance of single-source-precursor-synthesized SiCuCN-based ceramic nanocomposites. *J Adv Ceram* 2023, **12**: 1299–1316.
[54] Yu GY, Shao GF, Xu RP, *et al.* Metal-organic framework-manipulated dielectric genes inside silicon carbonitride toward tunable electromagnetic wave absorption. *Small* 2023, **19**: 2304694.
[55] Xu JJ, Wang L, Wang XM, *et al.* Research progress of high temperature absorbing materials. *Adv Ceram* 2024, **45**: 189–205. (in Chinese)
[56] Ma GS, Zhang KL, Yan YF, *et al.* Flower-branch-like carbon microtube/vanadium selenide: A highly efficient electromagnetic wave absorbing composite. *Chem Eng J* 2024, **495**: 152904.
[57] Zhang KL, Chen J, Yue SJ, *et al.* Facile synthesis of core–shell Cl/SiO_2 decorated RGO sheets composite for excellent electromagnetic wave absorption performance covering the whole X-band. *Compos Part A—Appl S* 2020, **130**: 105755.
[58] Zeng Q, Tian HQ, Jiang J, *et al.* High-purity helical carbon nanotubes with enhanced electrochemical properties for supercapacitors. *RSC Adv* 2017, **7**: 7375–7381.
[59] Zhang XC, Zhang X, Yuan HR, *et al.* CoNi nanoparticles encapsulated by nitrogen-doped carbon nanotube arrays on reduced graphene oxide sheets for electromagnetic wave absorption. *Chem Eng J* 2020, **383**: 123208.
[60] Liu PB, Zheng SY, He ZZ, *et al.* Optimizing integrated-loss capacities via asymmetric electronic environments for highly efficient electromagnetic wave absorption. *Small* 2024, **20**: 2403903.
[61] Liu PB, Gao S, Wang Y, *et al.* Metal-organic polymer coordination materials derived Co/N-doped porous carbon composites for frequency-selective microwave absorption. *Compos Part B—Eng* 2020, **202**: 108406.
[62] Liu PB, Gao S, Liu XD, *et al.* Rational construction of hierarchical hollow CuS@CoS_2 nanoboxes with heterogeneous interfaces for high-efficiency microwave absorption materials. *Compos Part B—Eng* 2020, **192**: 107992.
[63] Sun MX, Wang DR, Xiong ZM, *et al.* Multi-dimensional Ni@C–CoNi composites with strong magnetic interaction toward superior microwave absorption. *J Mater Sci Technol* 2022, **130**: 176–183.
[64] Zhang KL, Lv WX, Chen J, *et al.* Synthesis of RGO/AC/Fe_3O_4 composite having 3D hierarchically porous morphology for high effective electromagnetic wave absorption. *Compos Part B—Eng* 2019, **169**: 1–8.
[65] Cole KS, Cole RH. Dispersion and absorption in dielectrics I. Alternating current characteristics. *J Chem Phys* 1941, **9**: 341–351.
[66] Seyedian SM, Ghaffari A, Mirkhan A, *et al.* Manipulating the phase and morphology of $MgFe_2O_4$ nanoparticles for promoting their optical, magnetic, and microwave absorbing/shielding characteristics. *Ceram Int* 2024, **50**: 13447–13458.
[67] Sheykhmoradi S, Ghaffari A, Mirkhan A, *et al.* Dendrimer-assisted defect and morphology regulation for improving optical, hyperthermia, and microwave-absorbing features. *Dalton Trans* 2024, **53**: 4222–4236.
[68] Li B, Tian HY, Li L, *et al.* Graphene-assisted assembly of electrically and magnetically conductive ceramic nanofibrous aerogels enable multifunctionality. *Adv Funct Mater* 2024, **34**: 2314653.
[69] Shao GF, Guo LQ, Xu RP, *et al.* Carbon nanofiber aerogel microspheres with heterogeneous skin-core structure for broadband electromagnetic wave absorption. *Carbon* 2024, **228**: 119416.
[70] Cheng JY, Li Y, Raza H, *et al.* Cross-scale synergistic manipulation of dielectric genes in polymetallic sulfides from micropolarization to macroconductance toward wide-band microwave absorption. *Adv Funct Mater* 2024, **34**: 2405643.
[71] Huang XG, Yu GY, Quan B, *et al.* Harnessing pseudo-Jahn–Teller disordering of monoclinic birnessite for excited interfacial polarization and local magnetic domains. *Small Meth* 2023, **7**: 2300045.
[72] Geng TB, Yu GY, Shao GF, *et al.* Enhanced electromagnetic wave absorption properties of ZIF-67 modified polymer-derived SiCN ceramics by *in situ* construction of multiple heterointerfaces. *Rare Met* 2023, **42**: 1635–1644.
[73] Rezaei H, Soltani-Mohammadi F, Dogari H, *et al.* Plasma-assisted doping of pyrolyzed corn husk strengthened by MoS_2/polyethersulfone for fascinating microwave absorbing/shielding and energy saving properties. *Nanoscale* 2024, **16**: 18962–18975.
[74] Peymanfar R, Ahmadi A, Selseleh-Zakerin E, *et al.* Electromagnetic and optical characteristics of wrinkled Ni nanostructure coated on carbon microspheres. *Chem Eng J* 2021, **405**: 126985.
[75] Peymanfar R, Mousivand P, Mirkhan A. Fabrication of ZnS/g-C_3N_4/gypsum plaster nanocomposite toward refining electromagnetic pollution and saving energy. *Energy Technol* 2024, **12**: 2300684.
[76] Cao KY, Ye WP, Fang Y, *et al.* Construction of three-dimensional porous network Fe–rGO aerogels with monocrystal magnetic Fe_3O_4@C core–shell structure nanospheres for enhanced microwave absorption. *Mater Today Phys* 2024, **42**: 101383.
[77] Zhao Y L, Song Y Q, Ma X, *et al.* Preparation and wave absorbing performance of mullite–SiBCN coatings. *Adv Ceram* 2024, **45:** 259–267. (in Chinese)
[78] Huang XG, Wei JW, Zhang YK, *et al.* Ultralight magnetic and dielectric aerogels achieved by metal-organic framework initiated gelation of graphene oxide for enhanced microwave absorption. *Nano-Micro Lett* 2022, **14**: 107.
[79] Zhang Y, Yang SH, Xin Y, *et al.* Designing symmetric gradient honeycomb structures with carbon-coated iron-based composites for high-efficiency microwave absorption. *Nano-Micro Lett* 2024, **16**: 234.